# CFD modeling of multiphase flow in an alkaline water electrolyzer

Document license:
TAVERNE

DOI:
[10.1016/j.ces.2020.115926](https://doi.org/10.1016/j.ces.2020.115926)

Document status and date:
Published: 14/12/2020

Document Version:
Publisher's PDF, also known as Version of Record (includes final page, issue and volume numbers)

Please check the document version of this publication:

• A submitted manuscript is the version of the article upon submission and before peer-review. There can be important differences between the submitted version and the official published version of record. People interested in the research are advised to contact the author for the final version of the publication, or visit the DOI to the publisher's website.
• The final author version and the galley proof are versions of the publication after peer review.
• The final published version features the final layout of the paper including the volume, issue and page numbers.

[Link to publication](#)

# CFD modeling of multiphase flow in an alkaline water electrolyzer

A. Zarghami [a], N.G. Deen [a], A.W. Vreman [a,b,*]

[a] *Power and Flow Group, Department of Mechanical Engineering, Eindhoven University of Technology, Eindhoven, the Netherlands*
[b] *Nouryon, Research Development and Innovation, Process Technology, Deventer, the Netherlands*

## HIGHLIGHTS

- Euler-Euler simulation of the flow in a water electrolyzer for a range of current densities.
- Comparison of the simulated local gas fraction with experimental data from literature.
- Development of user-defined functions in Fluent was required in order to satisfy the momentum balance of the gas phase.
- Demonstration of the important role of the turbulent dispersion force.
- The effect of the turbulence model on the gas distribution.

## ARTICLE INFO

## ABSTRACT

The hydrodynamic properties of gas–liquid flows in water electrolyzers are of great practical interest since the local distribution of gas influences the amount of electrical energy required to produce hydrogen. We used the Euler-Euler model to simulate the multiphase flow in a water electrolyzer and compared the results to existing experimental data, for a range of current densities. Our study shows that if only the drag force and buoyancy force are incorporated in the model, the spreading of the gas layers formed at the electrodes is not accurately predicted. By adding the turbulence dispersion force to the model, reasonable agreement with the experimental data could be obtained for the higher current densities. The turbulence dispersion had to be implemented via user-defined functions, in order to obtain results that satisfied the momentum balance. In addition the effect of different turbulence models on the turbulent dispersion was investigated.

© 2020 Elsevier Ltd. All rights reserved.

## 1. Introduction

Hydrogen, as an energy carrier, is expected to play a key role in future energy systems of the world. It owes its popularity to the increase in the energy costs caused by the declining availability of oil reserves, production and supply (McGlade, 2012) and also to the concerns about global warming and climate changes, which are blamed on man-made carbon dioxide ($CO_2$) emissions associated with fossil fuel use (Norby and Luo, 2004). Hydrogen is classified as a clean fuel as it emits nothing except water at the point of use. Also, it can be produced using renewable energy (e.g., wind, solar, hydropower, etc.) which makes it quite attractive (Steinfeld, 2002).

Also, hydrogen is used as raw material in the chemical industry, and also as a reductor agent in the metallurgic industry. Hydrogen is a fundamental building block for the manufacture of ammonia (Lattin et al., 2006), and hence fertilizers, and of methanol, used in the manufacture of many polymers. Refineries, where hydrogen is used for the processing of intermediate oil products, are another area of use (Mueller-Langer et al., 2007). Moreover, hydrogen is used in buildings and power industries, where it could be mixed with natural gas or combined with CO emissions to produce syngas (Liu et al., 2010). Furthermore, hydrogen energy used by the transport sectors is growing, where it can provide low-carbon mobility through fuel-cell electric vehicles (Cheng et al., 2007).

Such a wide-ranging hydrogen consumption requires large scale hydrogen production. Hydrogen is usually produced by gasification and reforming of heavy oil (Sato et al., 2003), gasification of coal and petroleum coke (Trommer et al., 2005) and reforming of natural gas (Turner, 2004). Although water electrolysis is a mature technology and is one of the simplest ways to produce hydrogen (and oxygen), it still contributes to only a small fraction ($\sim 4\%$) of the world hydrogen production (De Souza et al., 2007). However in comparison to other methods, water electrolyser has the advantage of producing extremely pure hydrogen ($> 99.9\%$), ideal for

some high value-added processes such as the manufacturing of electronic components. Moreover, water electrolysis can be powered by renewable energy sources which results in zero $CO_2$ emission. Hence applications of water electrolysis are mostly limited to small-scale applications where large-scale hydrogen production plants are not accessible or economical to use, including marine, rockets, spacecrafts, electronic industry and medical applications (Santos et al., 2013; Zeng and Zhang, 2010). The challenges for expanding the use of water electrolysis are to reduce energy consumption and cost and maintenance, and, on the other hand, to

increase efficiency (by applying high temperature and high pressure operation), durability and safety of current electrolyzers.

An alkaline-water electrolyzer is a type of electrochemical cell that is characterized by having two electrodes (namely anode and a cathode) operating in a liquid alkaline electrolyte solution of potassium hydroxide (KOH) or sodium hydroxide (NaOH). In industrial alkaline water electrolysis, 20–40% KOH or NaOH aqueous solution is used as the electrolyte instead of pure water to overcome high resistivity of water to electricity. Alkaline electrolyzers operate via transport of hydroxide ions (OH$^-$) through
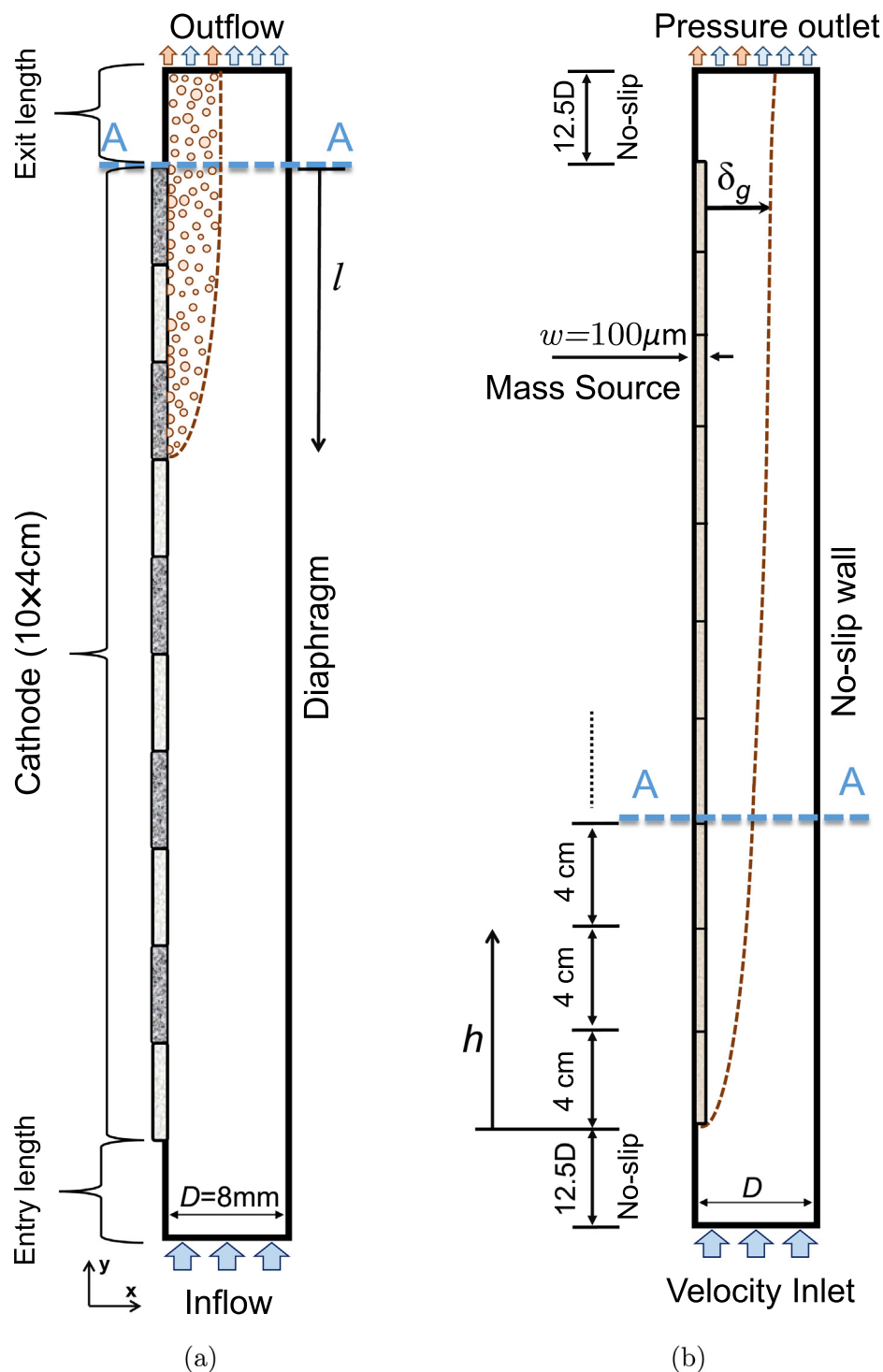


**Fig. 1.** a) Schematic of the cathodic half-cell, where hydrogen is produced, when three electrodes are active (i.e. $l = 12$ cm), and b) selected boundary conditions and computational parameters for simulations.

the electrolyte from the cathode to the anode with hydrogen bubbles being generated at the cathode and oxygen bubbles at the anode (see Fig. 1).

The performance of an alkaline-water electrolyzer is closely linked to the hydrodynamic characteristics of the gas–liquid flow in each cell. The presence of bubbles is known to cause local turbulence, which is very efficient in mixing and local distribution of the species. The bubbles form a curtain of increasing thickness along the vertical electrode (see Fig. 1). The rising bubbles also accelerate the electrolyte flow near the electrode which in turn pronounces the convective transport of electrochemically active species. On the other hand, in a zero-gap electrolysis cell the bubbles attached to the electrode reduce the effective electrode surface area (Vogt, 2012) while in nonzero-gap configurations the rising bubbles act as moving electrical insulators, thus affecting the current density distribution and increasing the ohmic drop across the cell (Hreiz et al., 2015). Hence, the hydrodynamic behaviour of the two-phase flow in an electrolysis cell can have a considerable effect on the cell efficiency.

It is worth mentioning that the bubble coverage, i.e. the fraction of the electrode surface covered by adhering bubbles, is an important operation parameter affecting the performance of the cell. Actually, bubbles adhering to an electrode surface insulate a part of the surface making it inactive in the electrochemical reaction, so that the current density and the surface overpotential at the bubble-free fraction of the surface is increased in case the total current is controlled to be constant. On the other hand, detaching bubbles from the electrode induce microconvection in the boundary layer intensifying mass transfer (Vogt, 2012; Vogt and Balzer, 2005).

Therefore, detailed investigation of bubble dynamics, phase interactions and gas hold-up is crucial for understanding the mechanism and enhances the performance of an electrochemical cell. There are numerous studies in the literature investigating various aspects of two-phase flow hydrodynamics in electrochemical cells (Hreiz et al., 2015; El-Askary et al., 2015; Abdelouahed et al., 2014a; Abdelouahed et al., 2014b). However, owing to the high gas fraction, many key features of the multiphase flow field cannot be captured by the common optical techniques. Hence, computational fluid dynamics (CFD) is also used for studying complex multiphase flow in electrochemical cells (Mat et al., 2004; Hreiz et al., 2015; Aldas, 2004; Hawkes et al., 2009; Alexiadis et al., 2011; Charton et al., 2010).

However, despite many interesting CFD studies available in the literature, validation of CFD results (such as hydrogen volume fraction and width of the gas hold-up in a cell) with equivalent experimental data is quite rare. Hence, there is as yet no consensus on the most capable and suitable method for simulating gas–liquid flow in an electrolyzer. In this way, ability of CFD models for predicting the width of the hydrogen bubbles curtain, which is an important feature of the flow, is a significant criterion for accuracy and reliability of the model. Accurate prediction of the bubble curtain spreading is quite challenging since if no bubble dispersion/transverse migration term is added to the CFD model, the distribution of local gas fraction cannot be predicted accurately (Caire et al., 2009; Abdelouahed et al., 2014b).

In this paper we aim to establish a CFD model to simulate multiphase flow in an alkaline-water electrolysis cell and compare the results with the experimental data. More particularly we focus on gas fraction and width of the bubble curtain in a cell. For this purpose the influences of drag and turbulent dispersion forces acting on the bubbles are analyzed to see the effect of each parameter on the flow pattern. To validate the modelling approach, numerical results are confronted to experimental data. The effects of interphase forces on the accuracy/stability of the CFD model as well as simulation results are also investigated. We also study some flow field parameters such as slip velocity, total amount of gas and turbulent viscosity in the system to better understand the physics of the problem. Finally, recommendations for a proper simulation of hydrogen generation in an electrochemical cell are presented.

The rest of paper is structured as follows. The details of the numerical model are presented in Section 2. Results are presented in Section 3, following by concluding remarks in Section 4.

## 2. The CFD model

### 2.1. Physical case

In this paper the experimental data achieved by Riegel et al. (1998) is used for validation purposes. The experimental setup consisted of two compartments, i.e. the cathodic and anodic compartments, which were separated by a diaphragm. The gases were evolved on ten electrode pairs mounted in the upper section of the electrolyser. Fig. 1a shows a sketch of the cathode cell where hydrogen was produced. The size of each electrode is 4 cm and they could be activated one by one, from top to bottom, indicating that the length of the cathode varied from $l = 4$ cm to $l = 40$ cm for different experiments. Also, measurements were performed for various current densities, i.e. $i = 500, 1500, 3250$ and $6250$ A/m$^2$. The width of the compartment was $D = 8$ mm and the potassium hydroxide solution (KOH) as the electrolyte was pumped through the electrolyser at $u_{in} = 0.69$ m/s. The gas fraction profile was measured at the upper end of the channel, just above the top electrode (see line $A - A$ in Fig. 1a). At that height a row of nine small platinum electrodes was mounted on a line perpendicular to the channel wall, so that, through the Maxwell equation, the gas fraction profile on that line was determined from the measured profile of the electrical resistance.

### 2.2. Governing equations

In this paper, the ANSYS Fluent® 19.1 package is used for simulating the multiphase flow. The flow is considered Newtonian, viscous, incompressible and isothermal as the physical properties of the phases remain constant. It is assumed that the operating pressure is 1 bar and the electrolyte is 30% KOH aqueous solution and $\rho_l = 1250$ kg/m$^3$ and $\mu_l = 0.9 \times 10^{-3}$ kg/m.s. Also, the gas phase is considered as a mixture of hydrogen and water vapor with $\rho_g = 0.21$ kg/m$^3$ and $\mu_g = 2 \times 10^{-5}$ kg/m.s (Haug et al., 2017; Takeuchi et al., 2008; Walker, 1971).

In the plane channel the transition from laminar to turbulent flow regime occurs at critical Reynolds number which is defined as $Re_{cr} = \rho_l u_{in} D / \mu_l \sim 2100$. Since the Reynolds number of the liquid in the cathode, $Re \sim 7600$ is considerably higher than the critical Reynolds number, the flow regime corresponding to the above mentioned experimental conditions is assumed to be turbulent. In order to represent the multiphase flow behavior we apply an Euler-Euler model which utilizes a set of momentum and continuity equations for each phase. The governing continuity and momentum equations according to the Eulerian model are (van der Hoef et al., 2006; van der Hoef et al., 2008)

$$\frac{\partial \alpha_g \rho_g}{\partial t} + \nabla \cdot (\alpha_g \rho_g \mathbf{u_g}) = \sigma_{V,g}, \tag{1}$$

$$\frac{\partial \alpha_g \rho_g \mathbf{u_g}}{\partial t} + \nabla \cdot (\alpha_g \rho_g \mathbf{u_g} \mathbf{u_g}) = \alpha_g \rho_g \mathbf{g} - \alpha_g \nabla p + \nabla \cdot (\alpha_g \mathbf{T_g}) + \mathbf{S} \tag{2}$$

for the dispersed phase, and

$$\frac{\partial \alpha_l \rho_l}{\partial t} + \nabla \cdot (\alpha_l \rho_l \mathbf{u_l}) = 0, \tag{3}$$

$$\frac{\partial \alpha_l \rho_l \mathbf{u}_l}{\partial t} + \nabla \cdot (\alpha_l \rho_l \mathbf{u}_l \mathbf{u}_l) = \alpha_l \rho_l \mathbf{g} - \alpha_l \nabla p + \nabla \cdot (\alpha_l \mathbf{T}_l) - \mathbf{S} \qquad (4)$$

for the continuous phase, where subscripts $g$ and $l$ refer to gas (dispersed) and liquid (continuous) phase, respectively. The symbols $\rho, \mu, \alpha$ and $\mathbf{u}$ represent density, dynamic viscosity, void fraction and velocity vector respectively. Note that, both phases are assumed to have a constant density. Also, $\sigma_{V,g}$ is a volumetric mass source that is only active in a thin layer adjacent to the electrode, so that no gas inlet boundary condition at the electrode is needed (see Section 2.4). Note that the pressure, $p$, is shared by the two phases in the Eulerian model. Also, the volume fractions are assumed continuous functions of space and time and their sum is equal to one, i.e. $\alpha_l + \alpha_g = 1$.

It can be seen that the Euler-Euler model has two continuity and two momentum equations for the two phases to calculate volume fraction and velocity fields of each phase and a shared pressure field. In this model, the phase volume fractions are assumed to be continuous functions of space and time and their sum is equal to one. In other words, as the densities of phases are assumed to be constant, the continuity equations provide governing equations for the phases volume fractions (i.e. $\alpha_g$ and $\alpha_l$), while both equations together with the constraint $\alpha_l + \alpha_g = 1$ lead to a Poisson equation from which the pressure is calculated.

In the governing equations, $\mathbf{T}_l$ denotes the stress tensor, which includes both viscous and turbulent stresses. Using Stokes' hypothesis for the second coefficient of viscosity, it is described for e.g. the viscous part of the liquid phase as

$$\mathbf{T}_l = 2\mu_l^{mol}\left(\mathbf{D}_l - \frac{1}{3}tr(\mathbf{D}_l)\mathbf{I}\right) - \rho_l \mathbf{R}_l, \qquad (5)$$

where $\mu^{mol}$ is the molecular dynamic viscosity, $tr$ represents the trace of matrix, $\mathbf{I}$ is the unit tensor and $\mathbf{D}_l$ is the strain rate tensor which is defined as

$$\mathbf{D}_l = 0.5(\nabla \mathbf{u}_l + (\nabla \mathbf{u}_l)^T). \qquad (6)$$

In Eq. 5, $\mathbf{R}_l$ is the Reynolds stress tensor which is defined in terms of the turbulent fluctuating velocities as $\mathbf{R}_l = <\mathbf{u}'_l\mathbf{u}'_l>$, where $<>$ makes the involved averaging operation explicit. This term can be modeled either by using the Boussinesq eddy viscosity hypothesis or by solving the Reynolds stress transport equation. In this work, the Reynolds stress equation (RSE) turbulence model is applied for modeling the stress tensor. This model accounts for anisotropy of the Reynolds stresses and is therefore often able to offer better accuracy than isotropic eddy viscosity-based turbulence models. Since the concentration of the gas phase is rather low, the dispersed turbulence model is used. Thus, the transport equations for turbulence quantities are only solved for the liquid phase, while $\mathbf{R}_g$, the Reynolds stress tensor of the dispersed (gas) phase, is simply proportional to $\mathbf{R}_l$ and the proportionality factor is computed according to the Tchen theory (Chan-Mou, 2013). The transport equation for the Reynolds stress tensor is calculated as (Pope, 2001; Wilcox, 2006)

$$\frac{\partial(\alpha_l \rho_l \mathbf{R}_l)}{\partial t} + \nabla \cdot (\alpha_l \rho_l \mathbf{u}_l \otimes \mathbf{R}_l) = \nabla \cdot (\alpha_l(\mu_l^{mol} + C_s \mu_l^{turb})\nabla \otimes \mathbf{R}_l)$$
$$+ \alpha_l \rho_l \left(\mathbf{P}_l + \phi_l - \frac{2}{3}\varepsilon_l \mathbf{I}\right), \qquad (7)$$

and the turbulent dissipation rate, $\varepsilon_l$, is given as

$$\frac{\partial(\alpha_l \rho_l \varepsilon_l)}{\partial t} + \nabla \cdot (\alpha_l \rho_l \mathbf{u}_l \varepsilon_l) = \nabla \cdot (\alpha_l(\mu_l^{mol} + C_\varepsilon \mu_l^{turb})\nabla \varepsilon_l)$$
$$+ \alpha_l \rho_l \frac{\varepsilon_l}{k_l}\left(C_{\varepsilon,1}\frac{1}{2}tr(\mathbf{P}_l) - C_{\varepsilon,2}\varepsilon_l\right), \qquad (8)$$

where $C_s, C_\varepsilon, C_{\varepsilon,1}$ and $C_{\varepsilon,2}$ are equal to 0.25, 0.15, 1.44 and 1.92 respectively. The tensor $\mathbf{P}_l = -2\mathbf{R}_l \cdot \mathbf{D}$ is the production by main shear, while the tensor $\phi_l$ represents the pressure-strain model formulated by Gibson and Launder (1978) and Launder (1989). Also,

the turbulent viscosity $\mu_l^{turb}$ is defined by $\rho_l C_\mu k_l^2/\varepsilon_l$, where $C_\mu = 0.09$ and $k_l = \frac{1}{2}tr(\mathbf{R}_l)$.

The last term $\mathbf{S}$ in the momentum equations of the phases represents the interphase momentum transfer which include the forces exerted on/by the dispersed phase. We consider this term as a summation of drag ($\mathbf{F}_d$) and turbulence dispersion ($\mathbf{F}_{td}$) forces:

$$\mathbf{S} = \mathbf{F}_d + \mathbf{F}_{td}. \qquad (9)$$

These forces play the most important role in predicting the distribution of the gas volume fraction. The wall-normal component of the force balance determines the establishment of radial distributions of the bubbles.

### 2.2.1. Drag force

The drag force represents a resistance to the movement of gas bubbles and acts in the opposite direction of the bubble–liquid slip velocity. The drag force is expressed as:

$$\mathbf{F}_d = -\frac{3}{4}\frac{C_d \rho_l \alpha_g}{d_b}|\mathbf{u}_g - \mathbf{u}_l|(\mathbf{u}_g - \mathbf{u}_l), \qquad (10)$$

where $\mathbf{u}_g - \mathbf{u}_l$ represents the rise (or terminal, relative) velocity vector between two phases, $d_b$ is the bubble diameter, $C_d$ is the drag coefficient, for which the so-called Schiller and Naumann correlation (Schiller, 1933) is employed here:

$$C_d = \begin{cases} \frac{24}{Re}(1 + 0.15Re^{0.687}) & \text{for } Re \leqslant 1000 \\ 0.44 & \text{for } Re > 1000 \end{cases}, \qquad (11)$$

where $Re$ is the Reynolds number of the bubble calculated on the basis of relative velocity as $Re = \rho_l|\mathbf{u}_g - \mathbf{u}_l|d_b/\mu_l$. The Schiller and Naumann model is a model for spherical particles. Since in the present case, the Eotvos number is low due to the small size of the bubbles, the bubbles are nearly spherical.

### 2.2.2. Turbulent dispersion force

Turbulent fluctuations produce randomness in the relative velocity between phases, which leads to oscillations in the drag force. While these fluctuations in the streamwise direction are low compared to the mean drag and buoyancy force, they bring a considerable impact on the redistribution of bubbles in the spanwise direction. This effect can be expressed as a turbulent dispersion force acting on the gas phase which signifies the turbulent dispersion of the bubbles by the random motion of continuous phase eddies. This is caused by the combined action of turbulent eddies and interphase drag which is derived by the volume fraction gradient and tend to flatten the volume fraction distribution (Ishii and Hibiki, 2010).

Burns et al. (2004) have derived a model for the turbulent dispersion force based on Favre averaging of the drag term, which is given by:

$$\mathbf{F}_{td} = -\frac{3}{4}\frac{C_d}{d_b}\alpha_g|\mathbf{u}_g - \mathbf{u}_l|\frac{\mu_l^{turb}}{Sc_{td}}\left(\frac{1}{\alpha_g} + \frac{1}{\alpha_l}\right)\nabla\alpha_g, \qquad (12)$$

where $Sc_{td}$ is the Schmidt number of turbulent dispersion with adopted value of 0.9. The proportionality to the gradient of the volume fraction in turbulence dispersion equation causes transport of gas from regions of high concentration to regions of low concentration. Physically this transport is due to local (turbulent) fluctuations of the velocities. Therefore this term is called the turbulent dispersion model.

### 2.2.3. Buoyancy force

The buoyancy is an upward force exerted by a fluid on bubbles in a gravity field. In fluids, pressure increases with depth; hence, when a bubble rises in a fluid, the pressure exerted on its bottom

surface is higher than the pressure exerted on its top surface. This difference in the pressure leads to a net upward force which opposes the gravity force. It is remarked that the buoyancy force acting on the bubbles is not included in **S** but included in the governing equations (see Eq. 2) as $\mathbf{F}_b = \alpha_g \rho_g \mathbf{g} - \alpha_g \nabla p$. This term is significant and positive in the vertical direction, while it is small in the horizontal direction.

### 2.3. Bubble size

The diameter of bubbles is a required input parameter. Hence, we have to prescribe a representative bubble size in order to numerically solve the problem. The size distribution of bubbles at the electrode depends on several parameters, such as number of nucleation sites, surface wettability, etc. Various experimental studies (Hreiz et al., 2015; Abdelouahed et al., 2014b; Boissonneau and Byrne, 2000; Hreiz et al., 2015; Vogt, 2012) have shown that there are three major phenomena that may change the bubble size significantly: (1) change in hydrostatic pressure applied to the bubbles during their rise, (2) mass transfer phenomena and incorporation of dissolved gas from the electrolyte and (3) bubble coalescence. However, the first phenomenon is only significant if the operating pressure is very low or if the cells height exceeds a few meters. Considering the operating conditions and geometry of the selected case study, we can safely ignore this phenomenon. The second phenomenon is also neglected because inclusion of mass transport of dissolved hydrogen is beyond the scope of this paper.

Flow visualizations have shown that (Abdelouahed et al., 2014b; Hreiz et al., 2015) bubble coalescence occurs in the vicinity of the electrodes only, and mainly among the bubbles that are not yet detached from the surface. However, the high ionic strength of electrolyte solutions, which is measure of the total concentration of ions in solution, is known to limit the significance of this phenomenon. For instance, it has been observed that a significant number of bubbles do not coalesce and maintain their initial small size (Boissonneau and Byrne, 2000; Hreiz et al., 2015). Hence, the phenomenon is far from being prevalent and we assume that there is no bubble coalescence and break-up. Therefore, a monodisperse bubble size distribution is a reasonable assumption for the purpose of this work.

Haug et al. (2017) measured the averaged bubble size as a function of current density for an alkaline-water electrolyzer at 80 °C with ∼ 30% KOH aqueous solution as the electrolyte. They showed that the mean cathodic bubble size diameter firstly grows from 170 to 220 μm in the range from $i = 100$ to $300$ A/m² and then decreases to an approximately constant value for $i > 1000$ A/m². Hence, according to data available in Haug et al. (2017), we set $d_b = 150$ μm for $i = 500$ A/m² and $d_b = 100$ μm for $i \geqslant 1000$ A/m².

### 2.4. Boundary conditions

The detailed geometry of the channel is shown in Fig. 1b. The velocity-inlet boundary condition is applied for the bottom boundary of the computational domain as a uniform velocity profile with $u_{l,y} = 0.69$ m/s, $u_{l,x} = 0, u_{g,y} = 0$ and $u_{g,x} = 0$. The inlet boundary is placed at a distance $12.5D = 10$ cm below the first electrode. We verified that this entry length was sufficiently large to obtain a fully developed mean velocity profile just below the first electrode. At the outlet boundary (at the top), a constant pressure is prescribed. In order to prevent upstream effects of the outlet boundary condition on the fluid flow, the boundary is placed 10 cm above the top electrode, so that the total height of the computational domain is 60 cm. All other boundaries are set as no-slip boundaries, for which the standard

wall function approach is applied (Pope, 2001; Launder and Spalding, 1983), which means that a model for the shear stress close to the wall is applied as wall stress condition in the momentum equation.

In order to simulate the bubble generation at the electrodes, a volumetric mass source for the gas phase is applied in a region adjacent to the left wall with a width equal to the diameter of the bubbles, i.e. $w = 150$ μm for $i = 500$ A/m² and $w = 100$ μm for $i \geqslant 1000$ A/m². Note that for each case the mesh is stretched in such a way that the width of the first cell becomes equal to the diameter of the bubbles. Thus the hydrogen produced by the reaction at the surface of electrode is prescribed as a volumetric mass source and not as a surface mass source (or horizontal inlet velocity). It should be highlighted that the latter was also tried, but it appeared to interfere with or deactivate the wall shear stress model needed in the standard wall function approach. Therefore, we have chosen the other route, the use of a volumetric source term. The volumetric source term is calculated as:

$$\sigma_{V,g} = C \frac{M_g F_g}{w},\qquad(13)$$

where $M_g$ and $F_g = i/Fz$ represent the molar mass (kg/mol) and mole flow (mol/m²s) of the gas mixture respectively, $i$ is the current density, $F = 96487$ A.s/mol is the Faraday constant, and $z = 2$ is the number of electrons involved in the electrochemical reaction ($2H_2O + 2e^- \rightarrow H_2 + 2OH^-$). Also, $C$ is a factor that accounts for the mole fraction $\chi_{H_2O}$ and $\chi_{H_2}$ in the gas phase at $T = 80$ °C. The water vapor pressure in the alkaline solution is approximately 0.26 bar, so that $\chi_{H_2O} = 0.26$ and $\chi_{H_2} = 0.74$ (Haug et al., 2017; Takeuchi et al., 2008; Walker, 1971). Therefore:

$$C = \frac{\chi_{H_2O} + \chi_{H_2}}{\chi_{H_2}} = \frac{1}{\chi_{H_2}} = 1.35.\qquad(14)$$

According to the above assumptions, the molar weight of the gas mixture is $M_g = 0.0062$ kg/mol and the volumetric source term for current density $i = 1500$ A/m² is equal to $\sigma_{V,g} = 0.652$ kg/m³s.

Note that in order to reduce the number of simulations that are required in this work, we simulate the electrolyzer with ten active electrodes. Then, the distribution of void fraction above the first electrode is compared with the experimental data for one pair of active electrodes, the profile of void fraction above the second electrode is compared with the experimental data for two (pairs of) active electrodes and so on. Our investigations showed that there are no significant differences between the results of the selected strategy and a strategy with multiple computational domains, in which each computational domain contains an electrode with a length equal to the total length of the number of active electrodes considered, whose total electrode length is precisely equal to the total length of number of active electrodes considered. Hence, we define a parameter, $h$, that represents the height along the 40 cm high electrode in the simulation, but at the same time $h$ also represents the distance from the bottom of the lowest active electrode in the experiment to the top of the highest active electrode, where experimental gas fraction was measured. Thus (simulation) results at height $h = 4N$ cm are compared with (experimental) results measured just above $N$ active electrodes (which have a total length of $l = h$). Also, the local gas layer thickness, $\delta_g$, is defined as a horizontal distance from the cathode surface to the point at which the gas void fraction is 0.001.

One of the important factors affecting multiphase flow behaviour is the slip velocity of bubbles which determines the momentum transfer between phases. In this work, the slip velocity is calculated as $\mathbf{U}_s = <\mathbf{u}_g - \mathbf{u}_l>$, where $<>$ indicates time averaging. Also, the total gas fraction is determined by the volume average of $\alpha_g$ as:

$$\alpha_{g,tot} = \frac{1}{V} \int \alpha_g dV, \qquad (15)$$

where $V$ is the volume of the entire flow domain.

## 2.5. Mesh dependency test

Since mesh refinement is a very important factor for determining an accurate solution, numerical tests were performed to determine the grid size for nearly grid-independent solutions for the

present problem. Three types of stretched meshes with different number of nodes in the cross-section direction, i.e. $N_x = 15, 30$ and 60 were used for $i = 1500$ A/m$^2$. The mesh size in the vertical (or streamwise) direction is uniform and is equal to $\Delta y = 2$ mm, $\Delta y = 1$ mm and $\Delta y = 0.5$ mm for $N_x = 15, 30$ and 60, respectively. The predicted gas volume fraction along $h = 24$ cm is shown in Fig. 2. As shown in the figure, the numerical results with $N_x = 60$ and $N_x = 30$ agree well with each other (differences less than 1%). Hence, the selected mesh size with $N_x = 30$ and $\Delta y = 1$ mm is a proper choice. This mesh is also used for the other current den-
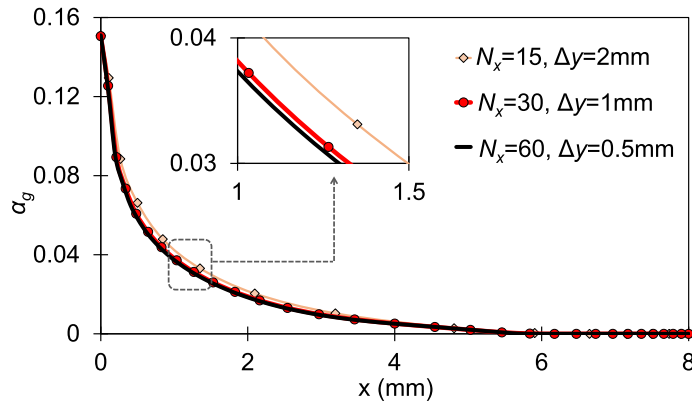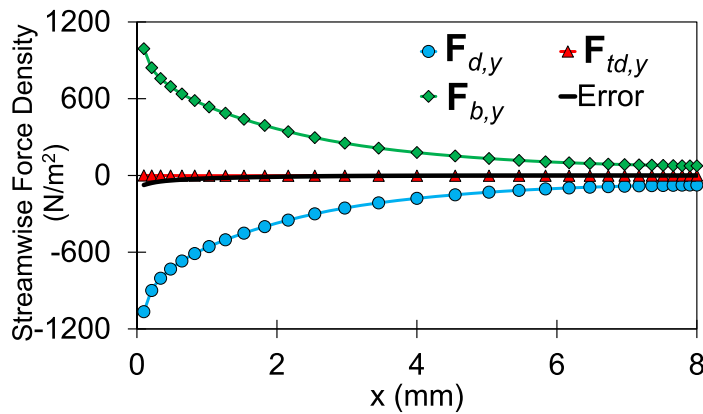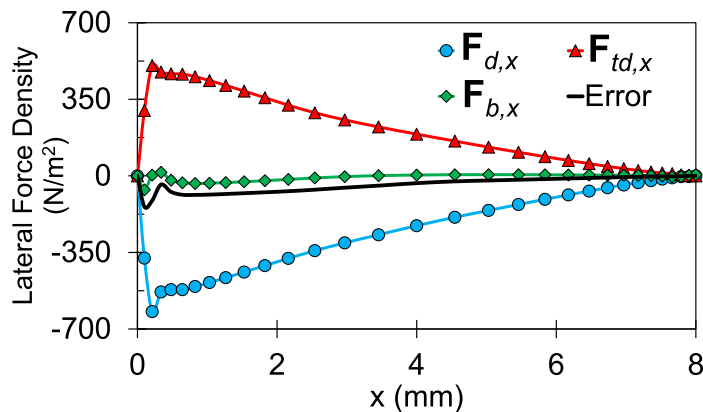


**Fig. 2.** Predicted gas volume fraction at $h = 24$ cm with various grid sizes for $i = 1500$ A/m$^2$.



**Fig. 3.** Distributions of a) streamwise ($\mathbf{F}_y$) and b) lateral ($\mathbf{F}_x$) components of force densities acting on bubbles along the cross-section of the channel at $h = 32$ cm when forces are selected as the default implementations in Fluent.

sities, except that for $i = 500$ A/m$^2$ the stretching factor was slightly modified (as explained in Section 2.4).

It is worth mentioning that the so-called QUICK scheme is chosen for spatial discretization of the governing equations. Also, the first-order implicit time stepping method is applied for temporal discretization.

### 2.6. Model verification

As we mentioned earlier, the Reynolds stress equation (RSE) model is applied as the turbulence model. The effects of various turbulence models on the simulation results will be discussed in the last part of Section 3. Here, the drag and the turbulence dispersion forces are considered as the major interaction forces between the phases. At first, these two forces were simply selected as they are available by default in Fluent. In order to verify the internal consistency of the model we check the momentum balance for the gas phase (see Eq. 2). For this purpose, the distributions profiles of the force components along the cross section of the channel at $h = 32$ cm with $i = 1500$ A/m$^2$ are plotted in Figs. 3 and 4. The convective, pressure gradient and viscous terms in the horizontal momentum equation are negligible compared to the forces and therefore not shown. It has been verified that the simulation reached the steady state and that the time derivatives in the momentum balance are negligible. Hence, the buoyancy, the drag and the turbulent dispersion forces are the remaining terms. For the gas momentum balance to be satisfied the summation of these three forces should be very close to zero, because the pressure gra-dient, convective and viscous terms are negligible. Any deviation from zero can be considered as error in the momentum balance.

Fig. 3 shows that the momentum balance in streamwise direction is not fully satisfied. Note that all simulation were well converged with residuals of all equations well below $10^{-5}$. The maximum error in the streamwise direction reaches 7% of the drag force in the vicinity of the electrode surface. However, there is a significant momentum imbalance in the lateral direction: the error reaches roughly 20% of the drag force in the region close to the electrode. Note that the error is calculated simply as the summation of the Buoyancy, drag and turbulent dispersion forces which should be very close to zero to show the satisfy the momentum balance.

It is mentioned that the amount of imbalance in the lateral direction is not the same for all cross-sections and it gets larger as the gas hold-up increases either by increasing the electrode size or by increasing the current density. Furthermore, it is mentioned that the imbalance was found to be at least as large when the RSE model was replaced by the $k - \varepsilon$ or SST $k - \omega$ model.

After doing extensive studies, we concluded that the turbulence dispersion force is not implemented as the formula presented in the Fluent manual or there is a kind of error in implementing this force in the source code of Fluent. To overcome this issue, we implemented user-defined-functions (UDFs) for both the Schiller-Naumann drag and the Burns turbulent dispersion forces according to equations described in the Fluent manual. Fig. 4 shows that the momentum balance is satisfied perfectly if the UDFs are used as momentum source terms and the default interfacial forces in Flu-



(a)

(b)
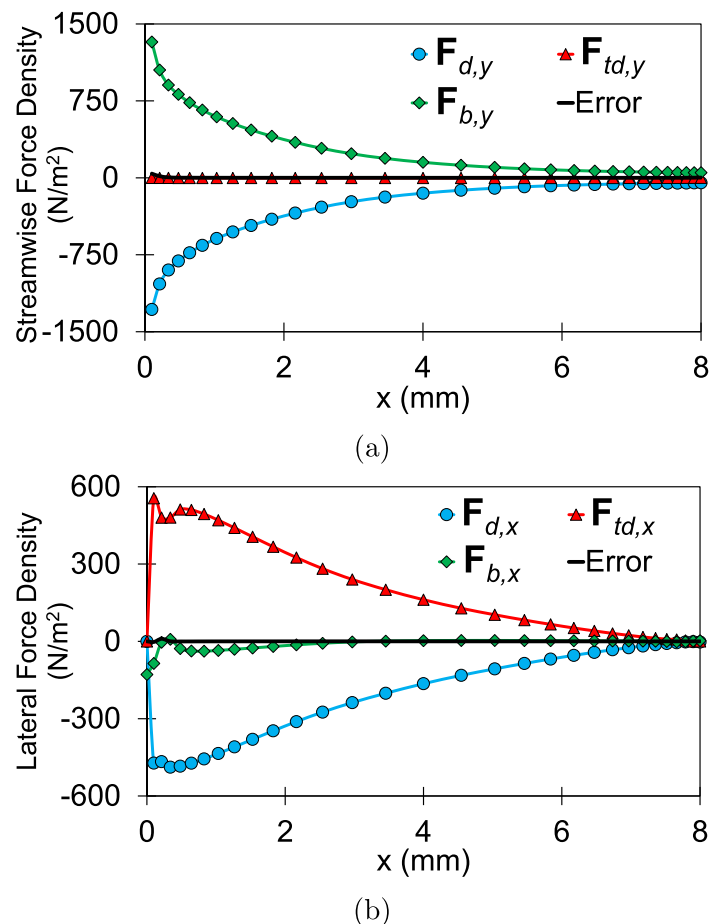
**Fig. 4.** Distributions of a) streamwise ($\mathbf{F}_y$) and b) lateral ($\mathbf{F}_x$) components of force densities acting on bubbles along the cross-section of the channel at $h = 32$ cm when forces are applied by using UDFs in Fluent.

ent are switched off: the sum of the forces is very close to zero at all points of both the streamwise and the lateral profiles. An equally good force balance was found when the UDF implementation was used in combination with the $k - \varepsilon$ or SST $k - \omega$ turbulence model.

Furthermore, we have performed simulations in which we switched on, in addition to the drag and turbulent dispersion forces, the default Fluent settings for the lift force, the wall lubrication and virtual mass forces. We added these forces to the model one by one. Our study showed that the wall lubrication force has insignificant influence on the spreading of the gas fraction in the channel. However, when the lift force or virtual mass force was added to the model, these forces affected the steady state gas fraction profiles in a spurious manner, as the steady state results
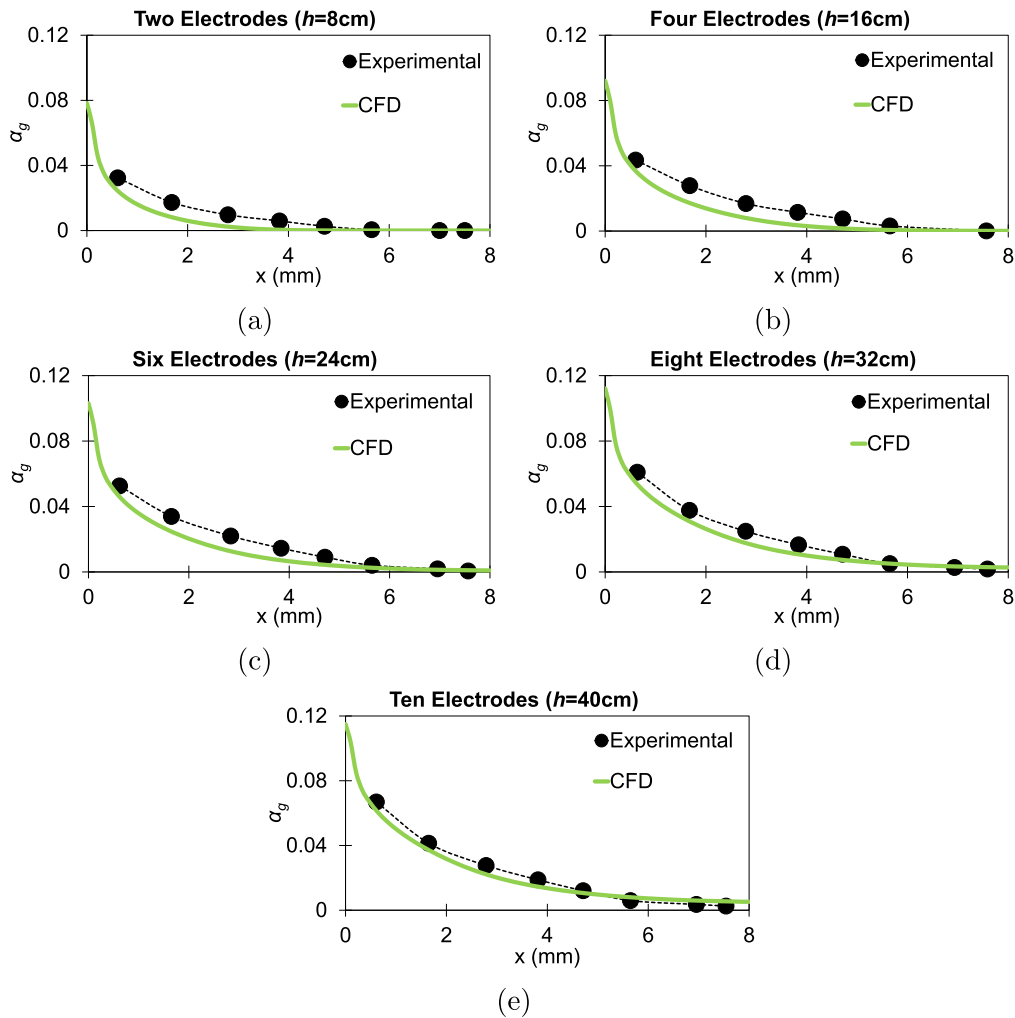


**Fig. 5.** Comparison of the predicted gas volume fraction with experimental data (Riegel et al., 1998) as a function of number of electrodes for $i$ = 1500 A/m².
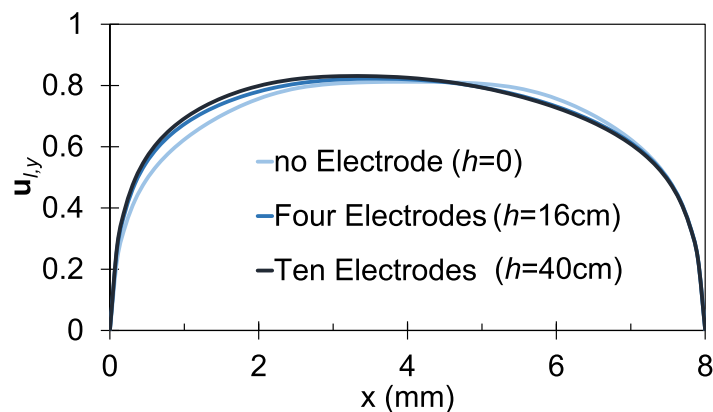


**Fig. 6.** Streamwise component of the liquid velocity for different number of electrodes and $i$ = 1500 A/m².
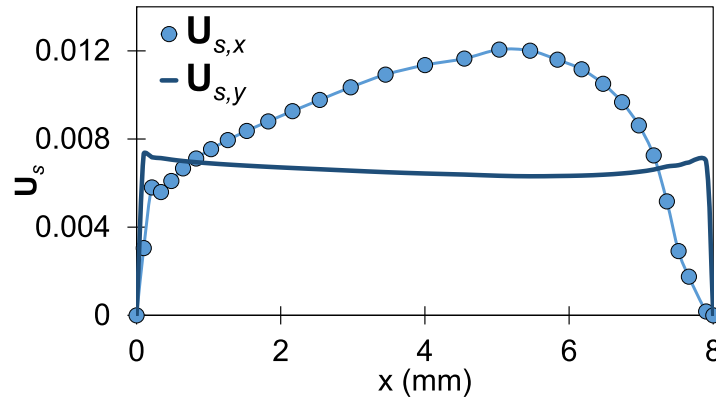
**Fig. 7.** Horizontal, $U_{s,x}$, and vertical, $U_{s,y}$ or streamwise, components of the slip velocity at $h = 24$ cm for $i = 1500$ A/m$^2$.
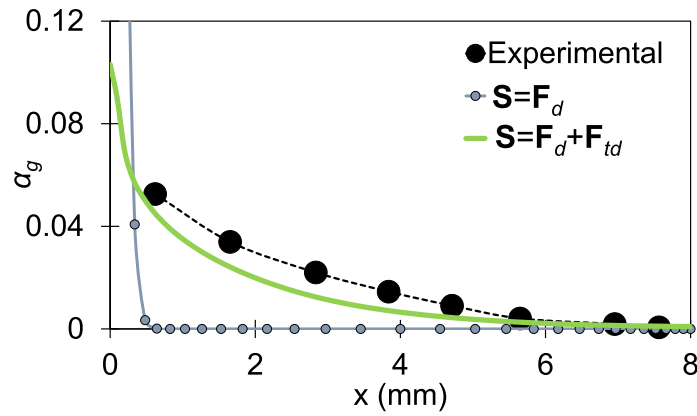


**Fig. 8.** Effect of drag only ($\mathbf{S} = \mathbf{F}_d$) and drag and turbulent dispersion forces ($\mathbf{S} = \mathbf{F}_d + \mathbf{F}_{td}$) on distribution of gas layer along the cross-section of the channel at $h = 24$ cm in the channel and $i = 1500$ A/m$^2$.
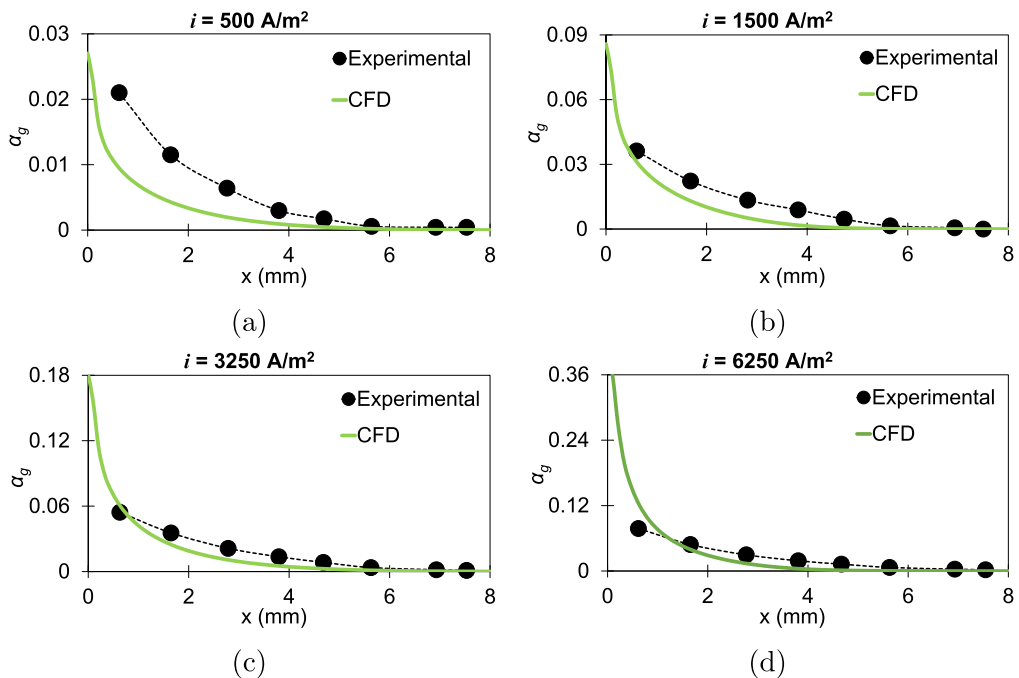


**Fig. 9.** Comparison between numerical volume fraction distribution of gas along the channel cross-section with the experimental data (Riegel et al., 1998) for different current densities .and $h = 12$ cm.

became dependent on the time step. These spurious effects did not disappear when the time step was reduced. Because of these issues, we decided to ignore these forces and include only the two most dominant forces, the drag and turbulent dispersion force, implemented as UDFs (as described above).

## 3. Results

The results of our simulations are compared with the experimental data of Riegel et al. (1998), who performed experiments for multiple current densities and for a multiple number of active electrodes. Simulations of some of these experiments were also presented in Mat et al. (2004) and El-Askary et al. (2015). However, in these references, the numerical results predicted for one active electrode (with the length of 4 cm) were compared with the experimental data obtained for three active electrodes (with the total length of 12 cm). Hence, a new attempt to simulate these experiments is clearly justified. It is worth mentioning that in Mat et al. (2004) a steady-state laminar flow has been solved for simulating two-phase mixture of the liquid and gas in a cell. Also, a mass diffusion term has been added to the continuity equation to model bubble dispersion. At the electrode surface, the velocity inlet boundary condition has been applied where the horizontal velocity component of gaseous phase is calculated using Faraday's law. In El-Askary et al. (2015), the Euler-Euler model coupled with $k - \varepsilon$ turbulent model has been used for simulating gas–liquid flow. The authors have applied Butler–Volmer type boundary condition for generating gas bubbles at the electrode.

In the next subsection, we show results for our base case, which corresponds to a current density and the RSE turbulence model. In the second subsection we show results for different current densities, while in the third subsection we include results for other turbulence models.

### 3.1. Results for the base case

Fig. 5 shows the predicted gas volume fraction distribution along the channel cross-section as a function of number of active electrodes for a current density $i = 1500$ A/m$^2$. The experimental data of Riegel et al. (1998) are also included. It can be seen that the CFD results are generally in reasonably good agreement with the measurements. The agreement becomes better if the number of active electrodes increases. The gas volume fraction attains a maximum value at the cathode and then decreases gradually along the cross-section of the channel as the channel becomes free of gas near the diaphragm surface. From this figure we also see that the gas volume fraction increases with the number of electrodes. This effect is more visible in close distances from the electrode. Also, the width of the gas volume fraction profile increases by activating a larger number of electrodes, which is due to the mixing and diffusion of the gas phase along the cell as a result of included non-drag forces.

The streamwise component of the liquid velocity as a function of number of electrodes is shown in Fig. 6. At the end of the entrance region, just below the electrodes (i.e. at $h = 0$), the velocity profile is symmetric and resembles a fully developed turbulent channel flow profile. Above this entrance region, electrodes are present, and by generating the gas they change the liquid velocity profile, which becomes asymmetric. The maximum shift toward the left, towards the location of the electrode surface at $x = 0$. In other words, the velocity near the surface of the electrodes is enhanced, because the bubbles accelerate the fluid. The bubbles are driven by the buoyancy force caused by the density difference between the phases. The rising bubbles, which are generated along the entire surface of the electrodes form a curtain of increasing width along the streamwise direction of the flow. For a larger number of active electrodes (larger $h$ in the simulations), the gas fraction is larger. This enhances the effect of buoyancy, so that the liquid velocity profile tends more toward the surface of the electrodes.

The distributions of streamwise ($\mathbf{F}_y$) and lateral (or cross-stream, $\mathbf{F}_x$) components of drag and non-drag force densities acting on bubbles were shown in Figs. 4a and 4b respectively. The negative sign of $\mathbf{F}_{d,y}$ indicates that the drag force acts in the negative $y$ direction. Due to the concentration of the gas bubbles in the vicinity of the cathode, $\mathbf{F}_{d,y}$ shows a peak value close to the electrode and then decreases gradually within the gas layer. The negative sign of $\mathbf{F}_{d,x}$ reveals that the gas bubbles experience a wall-directed force. This is caused by the positive horizontal slip velocity (see Fig. 7). The horizontal slip velocity is approximately the same as the horizontal gas velocity because the horizontal liquid velocity is negligible (absolute value less than 0.0002 at $h = 24$ cm). As shown in Fig. 7, the magnitude of the horizontal slip velocity is significant compared to the vertical one. The positive hori-
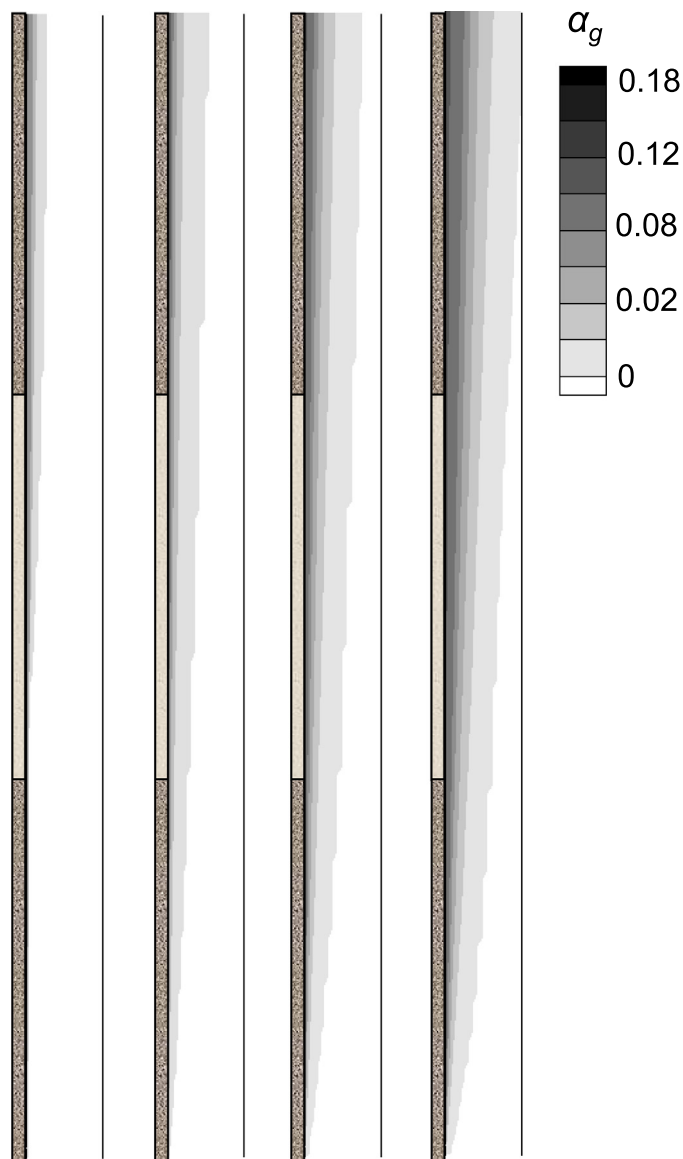


**Fig. 10.** Contour plots of the gas volume fraction in a cell with three active electrodes for different current densities, from left to right panels: $i = 500, i = 1500, i = 3250$ and $i = 6250$ A/m$^2$, respectively.

zontal slip velocity (or horizontal gas velocity) is caused by the positive turbulent dispersion force.

Fig. 4b shows that the lateral component of the turbulent dispersion force density, $F_{td,x}$, has a considerable value with a positive sign, whereas its streamwise component is negligible. The turbulent dispersion force has an important influence on the lateral gas fraction profiles in the electrolyzer as it expands the width of the gas layer.

The lateral component of the buoyancy force density is negligible, however the streamwise component, $F_{b,y}$, is significant. The balance between the buoyancy and the drag force determines the slip velocity of the bubbles. Since $F_{b,y}$ is proportional to the gas volume fraction, this force decreases with increasing distance from the electrode surface.

To further discuss the influence of turbulent dispersion forces on the hydrodynamics of the flow, we compare the distribution of the gas layer for two cases, i.e. $S = F_d$ and $S = F_d + F_{td}$, along the same cross-section. It is observed from Fig. 8 that by including only the drag force, i.e. $S = F_d$, the thickness of gas layer shrinks, which is due to the absence of the lateral component of $F_{td}$ that moves the bubbles away from the electrode. Hence, it means that effects of $F_{td}$ on the hydrodynamics of the flow are quite important. Inclusion of this force is required to predict the spreading of the gas layer sufficiently with reasonable accuracy.

### 3.2. Effect of current density

In this part, the effect of current density on the gas fraction distribution is discussed. Fig. 9 shows gas volume fraction profiles for different current densities along the cross-section of the channel with three electrodes (i.e. $h = 12$ cm). One can see that there is a reasonable agreement between the CFD results and the experimental data, apart from $i = 500$ A/m². It is clear that by increasing the current density the agreement between the CFD results and the experimental data improves.

As the electrochemical reaction rate is proportional to the current density, by increasing the current density the gas production rate rises, resulting in higher void fraction at the cathode surface. However, the void fraction at the cathode surface is not proportional to the increase in the current density due to thickening of the gas layer on the electrode. Increasing the current density results in a higher gas volume fraction, which on turn leads to more turbulent dispersion (the turbulent dispersion force is proportional to the gas volume fraction), so that bubbles move away from the electrode and the gas layer expands.

This is illustrated by Fig. 10, which shows contours of the gas volume fraction in the region $h \leqslant 12$ cm, for different current densities. If the current density increases, more gas is produced at the electrode and dispersed by the turbulence, so that both the local gas fraction as the total gas hold-up increase. The gas layer starts to grow at the leading edge at $h = 0$. We observe that the thickness of the gas layer as function of h has a small growth rate at low current density, but also that the growth rate increases if the current density increases. For the highest current density shown, the gas layer has spread across the entire channel width after three electrodes ($h = 12$ cm).

To quantify this further, we define the thickness of the gas layer, $\delta_g$, by the location where the gas fraction is less than 0.001. The
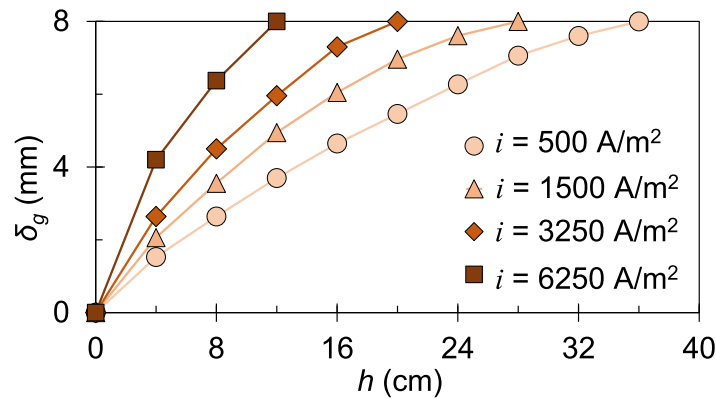


**Fig. 11.** The effect of height along the cathode on the thickness of the gas layers at different current densities.
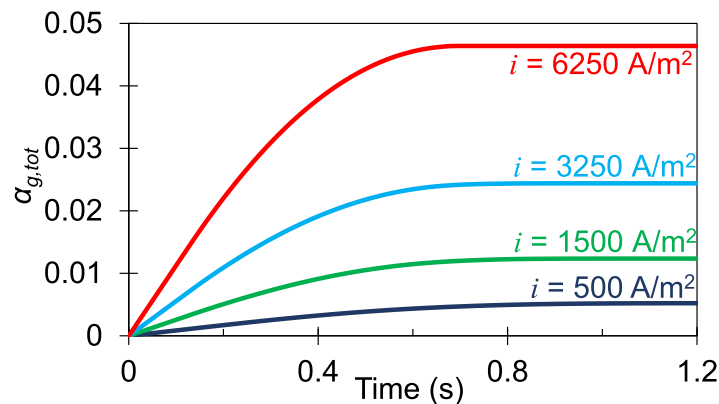


**Fig. 12.** Effect of current density on total volume fraction of gas in the electrolyzer.

thickness of the gas layer as function of height is shown in Fig. 11, also for different current densities. The growth rate of the gas layer is the slope of $\delta_g$ in this figure. As seen in Fig. 11, the thickness after nine electrodes ($h = 36$ cm) is equal to 8 mm for $i = 500$ A/m$^2$, whereas the gas layer reaches the diaphragm surface (i.e. $\delta_g$=8 mm) for $h \geqslant 28$ cm, $h \geqslant 20$ cm and $h \geqslant 12$ cm for $i = 1500$, $i = 3250$ and 6250 A/m$^2$, respectively. The predicted total volume fraction of the gas, $\alpha_{g,tot}$ in the cathode cell is shown in Fig. 12, which depicts that the total gas hold-up, the gas fraction averaged over the entire computational domain, is equal to $\alpha_{g,tot} = 0.5\%, 1.1\%, 2.4\%$ and $4.6\%$ for $i = 500$, 1500, 3250 and 6250 A/m$^2$, respectively.

### 3.3. Effect of turbulence models

In this section, we briefly present a comparative analysis of a few commonly used turbulence models for predicting the gas volume fraction in the channel. For this purpose, we use the standard $k - \varepsilon$ and the so-called SST $k - \omega$ models for turbulence modeling and compare the results with the RSE model.

Distributions of the gas void fraction along the cross-section of the channel at $h = 32$ cm predicted by the selected turbulence models are shown in Fig. 13a. Generally, the $k - \varepsilon$ model predicts a slightly lower gas fraction compared to the RSE model which is most evident at the electrode surface. This difference becomes lar-
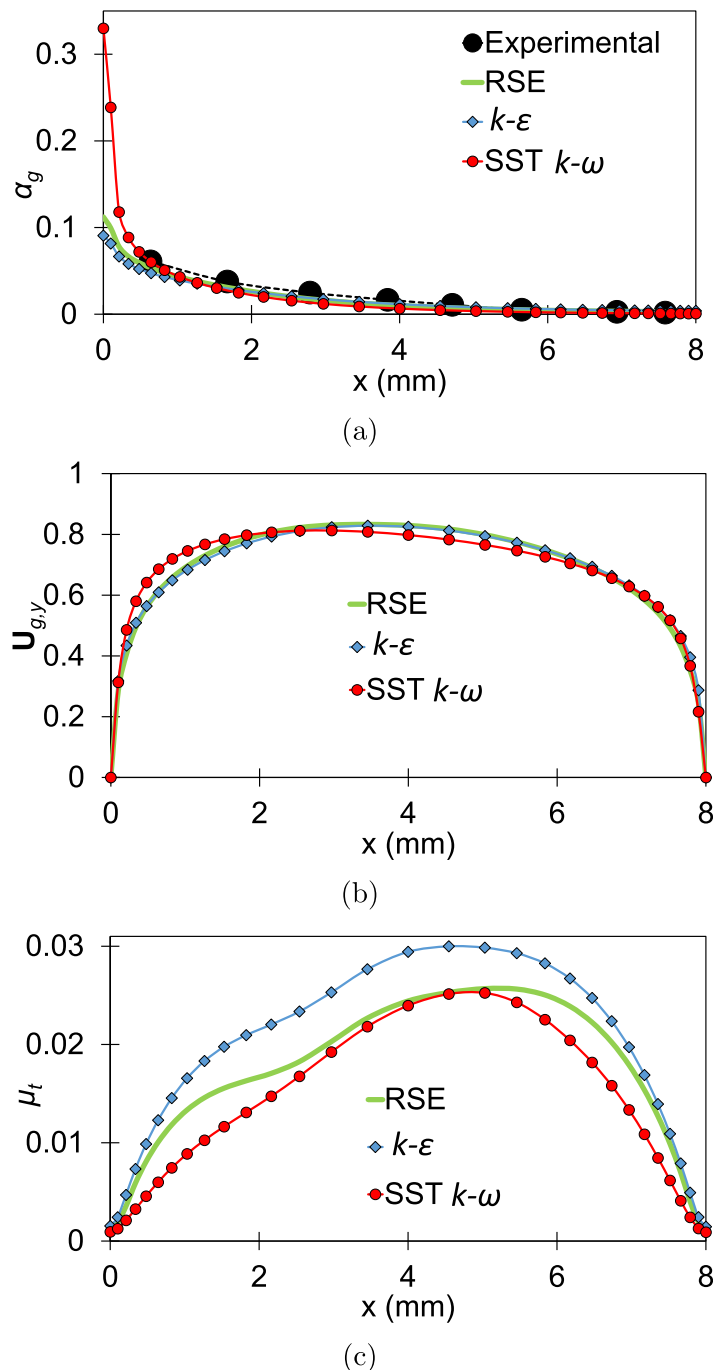


**Fig. 13.** a) Distribution of gas void fraction across $h = 32$ predicted by different turbulence models for $i = 1500$ A/m$^2$ and b) streamwise velocity of the gas phase and c) turbulent viscosity profiles along the cross-section of the channel.

ger at higher current densities. In contrast, the SST $k - \omega$ model predicts a much larger value for the gas fraction at the electrode compared to RSE model. Far away from the electrode, the SST $k - \omega$ predicts a lower gas fraction than the $k - \varepsilon$ model, so that both these models produce larger deviations from the experimental data than the RSE model does.

The streamwise component of the gas velocity for the selected turbulence models is shown in Fig. 13b. Compared to the RSE and $k - \varepsilon$ models, the gas velocity predicted by the SST $k - \omega$ model tends more toward the electrode surface due to the larger amount of gas predicted in the vicinity of the electrode. The distribution of the turbulence viscosity of the liquid phase predicted by each model is shown in Fig. 13c. It can be seen that the SST $k - \omega$ model results in smaller turbulence viscosity which in turn leads to lower dispersion of the gas phase and consequently a stronger accumulation of gas near the electrode as shown in Fig. 13a.

## 4. Conclusions

Accurate prediction of the gas volume fraction distribution is critical for understanding the hydrodynamics of the multiphase flow in electrolyzers. A wide variety of CFD modeling options is available, and there is not yet consensus on what the most suitable model is. Many available models suffer from a lack of generality and are highly dependent on tunable coefficients. In this paper we tried to predict and validate the hydrodynamics of gas–liquid flow in an electrolyser by including the effects of most important inter-phase forces, i.e drag, and turbulent dispersion forces. Our study showed that the turbulence dispersion force is of major importance for simulating the gas–liquid flow in an electrolyser, as without the turbulence dispersion force, the model is not able to predict the spreading of the gas layer in the cell correctly. Using user-defined versions for the drag and turbulence dispersion forces in the model, we computed gas void fractions across the channel for different heights of the electrode and also for various current densities, and we obtained fairly good qualitative agreements with experimental data from literature. The user-defined implementation of the forces was introduced in order to satisfy the gas momentum balance in Fluent. This balance was not satisfied when the standard built-in forces in Fluent were used. As the turbulence dispersion model relies on the model for the turbulent viscosity, a comparison of results obtained with different turbulence models was included. As a next step for the presented research, it is important to validate the Eulerian model at high gas volume fractions, but the main problem is to find/obtain detailed experimental data for these conditions.

## CRediT authorship contribution statement

**A. Zarghami:** Data curation, Formal analysis, Investigation, Methodology, Software, Validation, Visualization, Writing - original draft. **N.G. Deen:** Funding acquisition, Methodology, Resources, Supervision, Writing - review & editing. **A.W. Vreman:** Conceptualization, Formal analysis, Funding acquisition, Investigation, Methodology, Resources, Software, Supervision, Validation, Writing - review & editing.

## Declaration of Competing Interest

The authors declare that they have no known competing financial interests or personal relationships that could have appeared to influence the work reported in this paper.

## References

Abdelouahed, L., Hreiz, R., Poncin, S., Valentin, G., Lapicque, F., 2014a. Hydrodynamics of gas bubbles in the gap of lantern blade electrodes without forced flow of electrolyte: Experiments and cfd modelling. Chem. Eng. Sci. 111, 255–265.

Abdelouahed, L., Valentin, G., Poncin, S., Lapicque, F., 2014b. Current density distribution and gas volume fraction in the gap of lantern blade electrodes. Chem. Eng. Res. Des. 92, 559–570.

Aldas, K., 2004. Application of a two-phase flow model for hydrogen evolution in an electrochemical cell. Appl. Mathe. Comput. 154, 507–519.

Alexiadis, A., Dudukovic, M., Ramachandran, P., Cornell, A., Wanngård, J., Bokkers, A., 2011. Liquid–gas flow patterns in a narrow electrochemical channel. Chem. Eng. Sci. 66, 2252–2260.

Boissonneau, P., Byrne, P., 2000. An experimental investigation of bubble-induced free convection in a small electrochemical cell. J. Appl. Electrochem. 30, 767–775.

Burns, A.D., Frank, T., Hamill, I., Shi, J.-M., et al., 2004. The favre averaged drag model for turbulent dispersion in eulerian multi-phase flows. In: 5th International Conference on Multiphase Flow, ICMF, vol. 4, ICMF, pp. 1–17.

Caire, J., Espinasse, G., Dupoizat, M., Peyrard, M., 2009. A hydraulic model to simulate the hydrodynamics of a fluorine electrolyser. WIT Trans. Eng. Sci. 65, 23–34.

Chan-Mou, T., 2013. Mean Value and Correlation Problems Connected with the Motion of Small Particles Suspended in a Turbulent Fluid. Springer.

Charton, S., Janvier, J., Rivalier, P., Chamet, E., Caire, J.-P., 2010. Hybrid sulfur cycle for $H_2$ production: A sensitivity study of the electrolysis step in a filter-press cell. Int. J. Hydrogen Energy 35, 1537–1547.

Cheng, X., Shi, Z., Glass, N., Zhang, L., Zhang, J., Song, D., Liu, Z.-S., Wang, H., Shen, J., 2007. A review of pem hydrogen fuel cell contamination: Impacts, mechanisms, and mitigation. J. Power Sources 165, 739–756.

De Souza, R.F., Padilha, J.C., Gonçalves, R.S., De Souza, M.O., Rault-Berthelot, J., 2007. Electrochemical hydrogen production from water electrolysis using ionic liquid as electrolytes: towards the best device. J. Power Sources 164, 792–798.

El-Askary, W., Sakr, I., Ibrahim, K., Balabel, A., 2015. Hydrodynamics characteristics of hydrogen evolution process through electrolysis: Numerical and experimental studies. Energy 90, 722–737.

Gibson, M., Launder, B., 1978. Ground effects on pressure fluctuations in the atmospheric boundary layer. J. Fluid Mech. 86, 491–511.

Haug, P., Kreitz, B., Koj, M., Turek, T., 2017. Process modelling of an alkaline water electrolyzer. Int. J. Hydrogen Energy 42, 15689–15707.

Hawkes, G., O'Brien, J., Stoots, C., Hawkes, B., 2009. 3D CFD model of a multi-cell high-temperature electrolysis stack. Int. J. Hydrogen Energy 34, 4189–4197.

Hreiz, R., Abdelouahed, L., Fuenfschilling, D., Lapicque, F., 2015. Electrogenerated bubbles induced convection in narrow vertical cells: A review. Chem. Eng. Res. Des. 100, 268–281.

Hreiz, R., Abdelouahed, L., Fuenfschilling, D., Lapicque, F., 2015. Electrogenerated bubbles induced convection in narrow vertical cells: Piv measurements and euler–lagrange cfd simulation. Chem. Eng. Sci. 134, 138–152.

Ishii, M., Hibiki, T., 2010. Thermo-fluid Dynamics of Two-phase Flow. Springer Science & Business Media.

Lattin, W., Utgikar, V.P., 2006. Transition to hydrogen economy in the united states: a 2006 status report. Int. J. Hydrogen Energy 32, 3230–3237.

Launder, B.E., 1989. Second-moment closure and its use in modelling turbulent industrial flows. Int. J. Numer. Meth. Fluids 9, 963–985.

Launder, B.E., Spalding, D.B., 1983. The numerical computation of turbulent flows. In: Numerical Prediction of Flow, Heat Transfer, Turbulence and Combustion, Elsevier, 1983, pp. 96–116.

Liu, K., Song, C., Subramani, V., 2010. Hydrogen and Syngas Production and Purification Technologies. John Wiley & Sons.

Mat, M.D., Aldas, K., Ilegbusi, O.J., 2004. A two-phase flow model for hydrogen evolution in an electrochemical cell. Int. J. Hydrogen Energy 29, 1015–1023.

McGlade, C., 2012. A review of the uncertainties in estimates of global oil resources. Energy 47, 262–270.

Mueller-Langer, F., Tzimas, E., Kaltschmitt, M., Peteves, S., 2007. Techno-economic assessment of hydrogen production processes for the hydrogen economy for the short and medium term. Int. J. Hydrogen Energy 32, 3797–3810.

Norby, R.J., Luo, Y., 2004. Evaluating ecosystem responses to rising atmospheric $Co_2$ and global warming in a multi-factor world. New Phytol. 162, 281–293.

Pope, S.B., 2001. Turbulent flows.

Riegel, H., Mitrovic, J., Stephan, K., 1998. Role of mass transfer on hydrogen evolution in aqueous media. J. Appl. Electrochem. 28, 10–17.

Santos, D.M., Sequeira, C.A., Figueiredo, J.L., 2013. Hydrogen production by alkaline water electrolysis. Química Nova 36, 1176–1193.

Sato, S., Lin, S.-Y., Suzuki, Y., Hatano, H., 2003. Hydrogen production from heavy oil in the presence of calcium hydroxide? Fuel 82, 561–567.

Schiller, L., 1933. A drag coefficient correlation. Zeit. Ver. Deutsch. Ing. 77, 318–320.

Steinfeld, A., 2002. Solar hydrogen production via a two-step water-splitting thermochemical cycle based on zn/zno redox reactions. Int. J. Hydrogen Energy 27, 611–619.

Takeuchi, J., Satake, S.-I., Morley, N.B., Kunugi, T., Yokomine, T., Abdou, M.A., 2008. Experimental study of mhd effects on turbulent flow of flibe simulant fluid in circular pipe. Fusion Eng. Des. 83, 1082–1086.

Trommer, D., Noembrini, F., Fasciana, M., Rodriguez, D., Morales, A., Romero, M., Steinfeld, A., 2005. Hydrogen production by steam-gasification of petroleum coke using concentrated solar poweri. thermodynamic and kinetic analyses. Int. J. Hydrogen Energy 30, 605–618.

Turner, J.A., 2004. Sustainable hydrogen production. Science 305, 972–974.

van der Hoef, M.A., Ye, M., van Sint Annaland, M., Andrews, A., Sundaresan, S., Kuipers, J., 2006. Multiscale modeling of gas-fluidized beds. Adv. Chem. Eng. 31, 65–149.

van der Hoef, M.A., van Sint Annaland, M., Deen, N., Kuipers, J., 2008. Numerical simulation of dense gas-solid fluidized beds: a multiscale modeling strategy. Annu. Rev. Fluid Mech. 40, 47–70.

Vogt, H., 2012. The actual current density of gas-evolving electrodesnotes on the bubble coverage. Electrochim. Acta 78, 183–187.

Vogt, H., Balzer, R., 2005. The bubble coverage of gas-evolving electrodes in stagnant electrolytes. Electrochim. Acta 50, 2073–2079.

Walker, R.D. Jr., 1971. A study of gas solubilities and transport properties in fuel cell electrolytes.

Wilcox, D.C., 2006. Turbulence Modeling for CFD. Dcw Industries, Inc., La Canada, Ca.

Zeng, K., Zhang, D., 2010. Recent progress in alkaline water electrolysis for hydrogen production and applications. Prog. Energy Combust. Sci. 36, 307–326.